

Measurement of atmospheric muon angular distribution using a portable setup of liquid scintillator bars

Hariom Sogarwal and Prashant Shukla

Nuclear Physics Division, Bhabha Atomic Research Centre, Mumbai 400085, India,
Homi Bhabha National Institute, Anushakti Nagar, Mumbai 400094, India

E-mail: sogarwalhariom@gmail.com, pshuklabarc@gmail.com

Abstract. Measurements of cosmogenic particles at various locations and altitudes are becoming increasingly important in view of worldwide interests in rare signals for search of new physics. In this work, we report measurement of muon zenith angle distributions and integrated flux using a portable setup of four one-meter long liquid scintillator bars. Each scintillator bar is read out from both sides via photomultiplier tubes followed by an 8-channel Digitizer. We exploit energy deposition and excellent timing of scintillators to construct two dimensional tracks and hence angles of charged particles. We use liquid scintillators since they have an added advantage of pulse shape discrimination (PSD) which can be used for detecting muon induced particles. The energy deposition, time window of event and PSD cuts are used to reduce the random as well as correlated backgrounds. In addition, we propose three track quality parameters which are applied to obtain a clean muon spectrum. The zenith angle measurement is performed upto 60° . With our improved analysis, we demonstrate that a setup of 3 bars can also be used for quicker and precise measurements. The vertical muon flux measured is $66.70 \pm 0.36 \pm 1.50 /m^2/sr/s$ with $n = 2.10 \pm 0.05 \pm 0.25$ in $\cos^n \theta$ at the location of Mumbai, India (19°N , 72.9°E) at Sea level with a muon momentum above 255 MeV/c. The muon flux has dependence on various factors, the most prominent are latitudes, altitudes and momentum cut of muon so that portable setup like this can be a boon for such measurements at various locations.

Contents

1	Introduction	1
2	Experimental setups	3
3	Analysis methods	5
3.1	Time and position	5
3.2	Energy deposition	9
3.3	Pulse Shape Discrimination (PSD)	10
3.4	Track quality parameters	11
3.5	Energy calibration	13
4	Measurement of efficiencies	14
5	Monte Carlo simulation and geometrical acceptance	16
6	Muon flux measurements using different geometries	19
7	Results with systematic uncertainties and discussions	24
8	Summary and outlook	27

1 Introduction

The cosmic particles and their interactions with the Earth continues to be an active area of physics for many decades [1]. The precise measurements of cosmogenic particles at various locations and altitudes not only contains rich physics but is important in the context of searching for rare signals to answer many of the open problems of physics. The cosmic particles are produced in cosmological processes like Supernova, active galactic nuclei, pulsars, gamma ray bursts, the Sun and Big bang and are accelerated in an intergalactic field. The primary cosmic rays bombarding the Earth isotropically contain high energy protons, helium and a tiny fraction of higher-Z nuclei. The magnetic field of the Sun tends to exclude lower energy particles $E < 1$ GeV and during periods of high solar activity, less cosmic rays can reach the Earth. Earth's magnetic field also tends to exclude lower energy charged particles and thus their flux is more towards poles as compared to that at equator.

After entering the Earth atmosphere, the primary charged particles interact strongly with the nuclei of air molecules (mainly oxygen and nitrogen) in the upper part of atmosphere and produce showers of secondary particles containing mostly pions and kaons plus other particles like hyperons, charmed particles and nucleon-antinucleon pairs [2, 3]. The neutral pions decay to two photons and the charged pions and kaons mostly decay to muons and neutrinos. Thus, the bulk of particles reaching the Earth surface contains neutrinos and muons. Although both are closely linked, the former are least interacting and the later undergo Coulomb interactions with the matter. The muons are the most abundant energetic charged particles with a mean energy of about 2 GeV at Sea level and are of immense use in testing and calibrating detectors for experimental high energy physics. The muon zenith angle (θ) distribution at Earth is observed to follow a distribution $I(\theta) = I_0 \cos^n \theta$, where I_0

is the vertical muon flux and the exponent n is ~ 2 [4]. The parameters I_0 and n depend on momentum cut off, latitude and altitude. Measurements of muon flux have been performed at many locations with varying altitudes right from the time cosmic rays were discovered.

Some of the early measurements of muon flux in the world are Hayman et al. (Durham, UK) [5], Greisen [6], Judge and Nash [7] and Crookes and Rastin [8]. Barbouti and Rastin [2] measured the muon flux at Nottingham, UK using flash tubes and Gieger counters in 1983. Haino et al. measured the energy distribution of muons at Tsukuba, Japan [9]. Fukui et al. [10] performed the measurements at geomagnetic latitude 24°N . Allkofer et al. [11] measured the muon flux at latitude 9°N . The charge ratio of atmospheric muons is of considerable physics interest and there are recent measurements like Agafonova et al. [12].

In India, the measurements of muon flux have been done at few places. Gokhale et al. [2] in 1993 measured the muon flux in Delhi (28.7°N) using GM counter telescope. In 1973, Karmakar et al. [13] measured the flux in Darjeeling (16°N) using plastic scintillator paddles. Sinha and Basu [14] measured muon flux using a multiplate cloud chamber in Kolkata (22.57°N) in 1959. De et al. [15] measured muon flux using an array of Gieger counters and scintillators in Kolkata (22.57°N) in 1972. Recently, Pethuraj et al. [16] performed the measurement using a setup of 12 layers of Resistive Plate Chambers (RPCs) at Madurai which is close to the proposed site for India based Neutrino Observatory (INO). Pal et al. [17] measured the muon flux in Colaba, Mumbai using a setup of 12 layers of RPCs. A country like India covers a wide range of latitudes ranging from Srinagar (34.08°N , 74.80°E) to Kanyakumari (8.09°N , 77.53°E) and this requires systematic measurements within India itself. In addition, many of the muon measurements are old and with the development of newer techniques in detectors and electronics, a revisit to the measurements is warranted.

In recent times, a lot of experiments have been done using plastic scintillators paddles/bars to measure muon flux. Wu et. al [18] used plastic scintillators to measure muon flux at various underground depths in China. Recently, four plastic scintillators were used to measure the muon flux at an underground laboratory at Jaduguda, India [19]. Work in Ref. [20] uses large area plastic scintillator and gives the energy spectra of passing and stopping muons and decay electrons/positrons at ground and at depth. There are several recent works using plastic scintillators to measure muon angle distributions using plastic scintillator bars [21, 22]. But setups using both energy and timing properties of scintillator bars for constructing clean muon tracks and effectively using them for zenith angle distributions are scarce. The work in Ref. [23] constructs muon tracks using two scintillator bars read out from both ends. The position in each bar was obtained using time difference between two ends of the bar, albeit with a poor position resolution. We employ liquid scintillator bars to measure the muons. This is done with a future aim of using the same setup for muon induced neutrons and spallation particles exploiting the pulse shape discrimination (PSD) property of liquid scintillators. To measure muon signal, a lower energy threshold is applied on all scintillators which removes bulk of the background and an additional cut on PSD improves the signal to background slightly more. Liquid scintillators have the advantage that they offer uniformity of scintillating solutes in the organic liquid. One practical drawback of using the liquid scintillators is horizontal level across the length of the bar is to be maintained. The rise time of liquid scintillators is slightly higher than the plastic scintillators.

In this work, we perform measurement of muon flux and angular distributions using a portable setup of four one-meter long liquid scintillator bars. Each scintillator bar is read out from both sides via photomultiplier tubes followed by an 8-channel Digitizer. We implemented several innovative ideas in the measurement. Position calibration of scintillator

bars is performed using vertical cosmic muons constrained by placing the four scintillator bars in cross positions. We also explore less time consuming methods to connect the position with the measured time. Energy calibration of detectors has been done using muons tracks with different angles travelling different pathlengths in the detector. The energy deposition, time window of event and PSD cuts are used to reject the backgrounds. In addition, three track quality parameters are proposed which are applied to obtain a clean muon spectrum. We optimize the distances between the bars so as to have larger zenith angle coverage keeping a good angular resolution. The setup can distinguish downgoing and upgoing tracks. The acceptance of all the geometries is obtained by Monte Carlo simulations using inputs from measured energy distributions. The efficiencies of all the cuts are measured using experimental methods. The correction in 2D track angles due to finite ϕ coverage has been done via simulation. The setup can easily be used for studying the interaction of muons with materials and can detect produced photons, protons and neutrons.

The paper is organized as follows. After an Introduction, Section 2 describes the experimental setups. Section 3 describes analysis methods in detail which includes calibration of different parameters and track reconstruction. Section 4 presents the methods to obtain the efficiencies of different cuts. Section 5 gives MC simulation used in the analysis. The measurements via various geometries are described in Section 6 and the results with systematic and statistical uncertainties are described in Section 7. Finally, we summarize in section 8.

2 Experimental setups

To measure the muon flux at sea level, a setup of four liquid scintillator bars placed in the same vertical plane is used. Each detector bar is 1.02 meter long and with a cross section 4.9 cm (height) \times 5.6 cm (width) of active material. Each bar consists of Organic liquid scintillator EJ301 (density 0.874 gm/cm³) enclosed inside a cuboidal aluminum casing with glass window at each end which were coupled to the photomultiplier tubes using optical gel. The PMTs used are from Electron Tubes Enterprises Ltd with model number 9214KA which have diameter 51 mm with blue-green sensitive bialkali photocathode and 12 high gain high stability dynodes of linear focused design. We use the energy, time and shape of the pulse in the measurements. Anode of PMT acquires an amplified negative signal which is fed to the attenuator and then to Digitizer DT5730. The CoMPASS Software is used to store the integrated energy in Long and Short gates and a time stamp for signals in each individual channel. Later we use an offline algorithm to reconstruct and analyze muon tracks. Here 25 ns time width is taken for searching the events in 8 signals. Later, after the time calibration we constrain the time difference of events between bottom and top detectors within 7 ns. For Close geometries we reduce this window to 5 ns.

Figure 1 shows the block diagram of the experimental setup with the data acquisition scheme. Figure 2 shows the experimental setup of 4 liquid scintillator bars in Square geometry. Figure 3 shows the picture of 8-Channel Digitizer (DT5730) along with a typical digitized pulse (ADC channel number as a function of time (ns).) from liquid scintillator. The Long and Short gates timings are also shown which will be used to integrate the charge of pulse within their time width. The time widths of Long and Short gates for charge integration are given in Table 1 and the discriminator parameters are given in Table 2. The value of Short gate is taken as 20 ns and is changed to 24 ns for Small and Close geometries. The acquisition rate in each channel \approx 80 Hz.

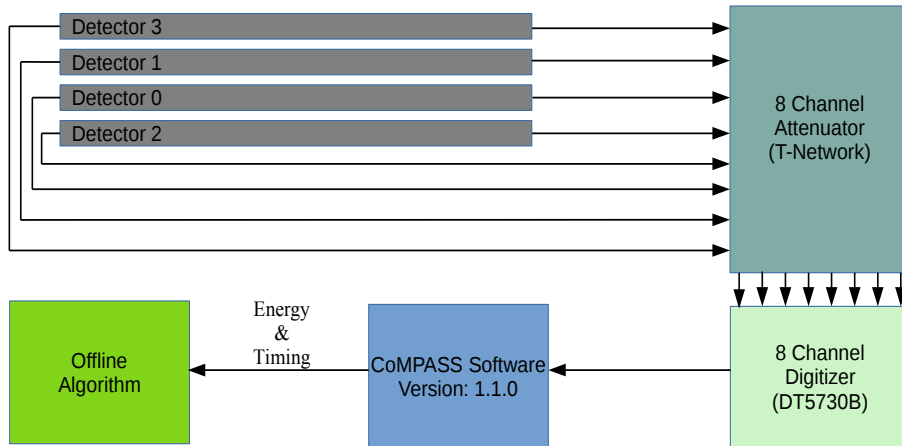


Figure 1. Block diagram of the experimental setup with the data acquisition scheme.



Figure 2. Experimental setup of 4 liquid scintillator bars in Square geometry.

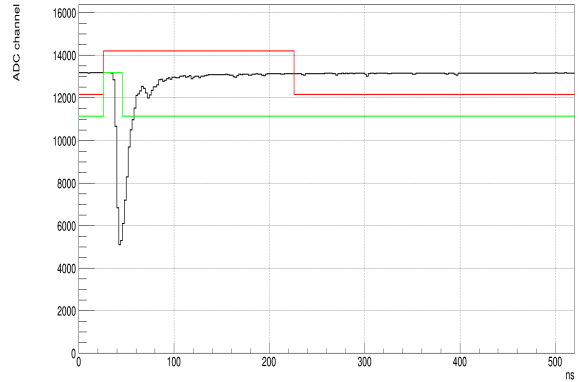


Figure 3. Picture of 8-Channel Digitizer (DT5730) along with a typical digitized pulse (ADC channel number as a function of time (ns.)) from liquid scintillator.

Table 1. Digitizer QDC Section.

Parameter	Values
Energy coarse gain	$10fC/(\text{LSB} \times V_{pp})$
Gate	200 ns
Short gate	20/24 ns
Pre-gate	70 ns

Table 2. Digitizer Discriminator Section.

Parameter	Values
Discriminator mode	CFD
Threshold	400 lsb
Trigger holdoff	1024 ns
CFD delay	6 ns
CFD fraction	75%
Input Smoothing	2 samples

We have used many geometries of the four detector bars in our setup. We first assign numbers 0, 1, 2, and 3 to the four bars used in the setup to explain each geometry. In all geometries, the sequence of detectors arranged from top to bottom is (3,1,0,2) except in geometry G_{13} and G_{15} where the position of upper two detectors and lower two detectors are interchanged from (3,1,0,2) to (1,3,2,0). Geometries G_{13} and G_{14} are called Square geometries since the distance between centers of top and bottom bars is about 95 cm, roughly equal to the length of the bars. The inter detector distances are kept almost equal. The physical picture of this geometry G_{14} , is given in Fig. 2. Geometry G_{11} corresponds to an increased distance of the top detector from bottom detector to 110.7 cm is called Large geometry. In geometry G_{17} , we squeeze the setup such that the distance between the top and bottom detectors is 63.6 cm keeping the inter detector distances equal. This is referred to as Small geometry. Close geometries G_{15} and G_{16} are used to measure the efficiencies of the detectors where the separation between two bars is kept very small as 3.2 cm. Table 3 shows the vertical distances which are measured (from detector centers) from the bottom detector and calculated time taken by a light ray to traverse the vertical paths from the top detector in the various geometries.

3 Analysis methods

3.1 Time and position

The most important parameter in the measurements is the time difference between the two ends of a detector which will finally be used for position measurement. In addition, the

Table 3. The vertical distances (which are measured from center to center from the bottom detector) and calculated time taken by light in the setups (which are calculated from the top detector).

Geometry	Distance/Time	Det₃	Det₁	Det₀	Det₂
G_{14} (Square)	Distance (cm)	95.0	63.3	31.8	0.0
(3,1,0,2)	Time (ps)	0.0	1056.6	2106.6	3166.6
G_{13} (Square)	Distance (cm)	63.3	95.0	0.0	31.8
(1,3,2,0)	Time (ps)	1056.6	0.0	3166.6	2106.6
G_{11} (Large)	Distance (cm)	110.7	63.2	31.7	0.0
(3,1,0,2)	Time (ps)	0.0	1583.3	2633.3	3690.0
G_{17} (Small)	Distance (cm)	63.6	42.4	19.45	0.0
(3,1,0,2)	Time (ps)	0.0	706.7	1471.7	2120.0
Efficiency setups (Close setups)					
G_{15} (Close)	Distance (cm)	18.5	27.8	0.0	9.2
(1,3,2,0)	Time (ps)	310.0	0.0	926.7	620.0
G_{16} (Close)	Distance (cm)	27.8	18.5	9.2	0.0
(3,1,0,2)	Time (ps)	0.0	310.0	620.0	926.7
Position calibration setup					
G_{Cross}	Distance (cm)	31.5	21.5	12.0	0.0
(3,1,0,2)	Time (ps)	0.0	333.3	650.0	1050.0
Background setups					
Described in the result section					

average time of the two sides of a detector is used as time arrival of the signal in that detector and will be used for inter detector time difference which is very useful to define a time window of an event and to know the directionality of track. Figure 4 shows the distributions of time difference between two ends of a detector, for each of the 4 detectors for the case of muons in the Square geometry G_{14} for (a) Detector 0 (b) Detector 1 (c) Detector 2 and (d) Detector 3. The events are filled under the coincidence in all 4 detectors within 7 ns time from top to bottom detectors under finalised cut conditions which are explained in next section and we produce the values here. The minimum energy deposition cut $E_{cut}=600$ ChNo. (8.07 MeV) and the conditions on track quality parameter used are $\chi^2/NDF < 3$, $\Delta t_{rms} < 0.9$, $E_{rms} < 0.2$ and $PSD < 0.78$. Time difference distributions are concentrated more towards centers in detector 0 and 1 as they are kept in the middle of the setup.

We use vertical muons to get the position time relation using two bars kept in cross position to the other two bars all in coincidence and then moving two of them to change the position. Figure 5 shows the Cross geometry G_{Cross} of four detectors seen from two perpendicular sides which are used to determine the time corresponding to muon positions in the overlap region of detectors (5.6 cm \times 5.6 cm). The detectors are arranged in sequence (3,1,0,2) from top to bottom.

Figure 6 shows the measured time for muon events at 11 different positions (center of overlap area) of the detector given in cm as (-48.0, -40.1, -30.1, -20.1, -10.0, 0.0, 10.0, 20.1, 30.2, 40.3, 48.0). Here 11 histograms are plotted on a single canvas. Figure 7(a) shows the measured time resolution σ_t using vertical muons which is 383 ps. This corresponds to a position resolution of ≈ 3 cm from a single bar which is reduced to 1.5 cm when we use four

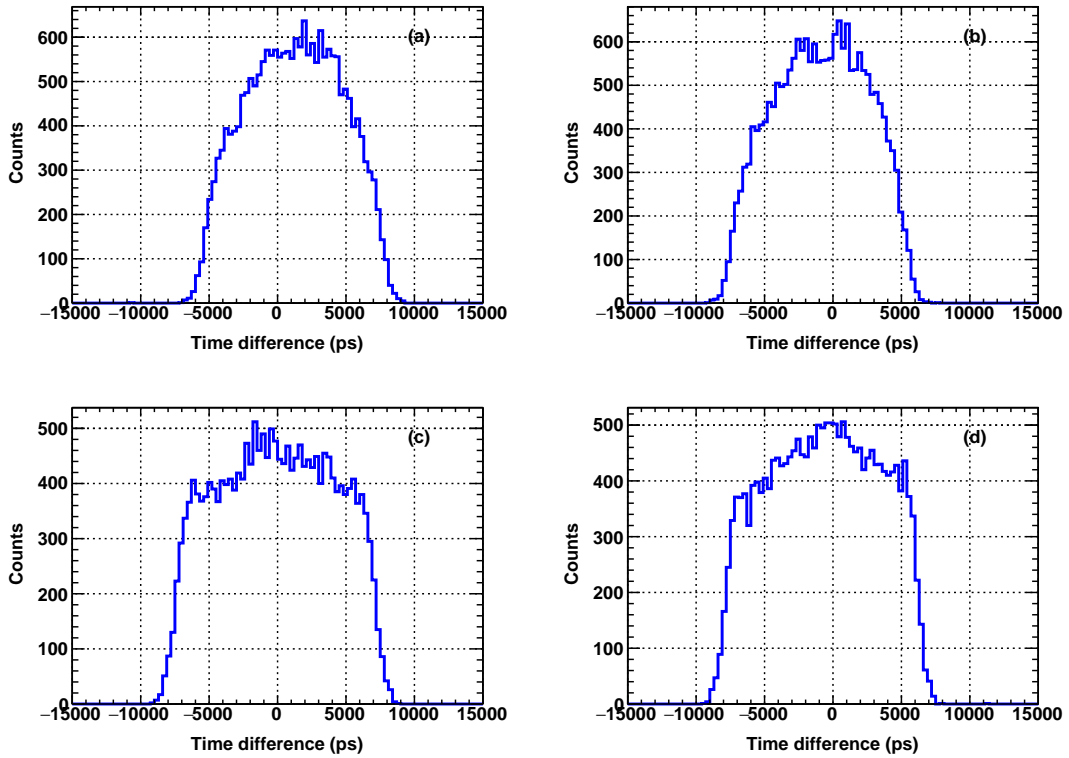


Figure 4. Distribution of time difference between two ends of a detector, for each of the 4 detectors for the case of muons in the Square geometry G_{14} . (a) Detector 0 (b) Detector 1 (c) Detector 2 and (d) Detector 3. The events are under finalised cut conditions.



Figure 5. Cross geometry G_{Cross} of four detectors seen from two perpendicular sides used to determine the time corresponding to muon positions in the overlap region of detectors ($5.6 \text{ cm} \times 5.6 \text{ cm}$). The detectors are arranged in sequence (3,1,0,2) from top to bottom.

bars for tracking. Figure 7(b) shows the measured time difference plotted as a function of position of muon in scintillator bars at 11 positions. The solid line is a fit to 11 points obtained as $t(\text{in ns}) = 0.143 \times y(\text{in cm}) - 0.725$. The dashed line is a fit to three points (middle point and 2 last points) shown by blue circle which is obtained as $t(\text{in ns}) = 0.140 \times y(\text{in cm}) - 0.757$. The two lines give two calibrations for position and time which are then included in systematics uncertainties in flux measurements. Two black points at $\pm 50 \text{ cm}$ are the points where the time difference distributions between two ends of a detector (of Figure 4) fall to 50% of their top value. These points fall on the fitted lines and hence can also be used as a quick alternative method to obtain time-position calibration.

Table 4 first row shows the time correction for the center of each detector. Table 4 second

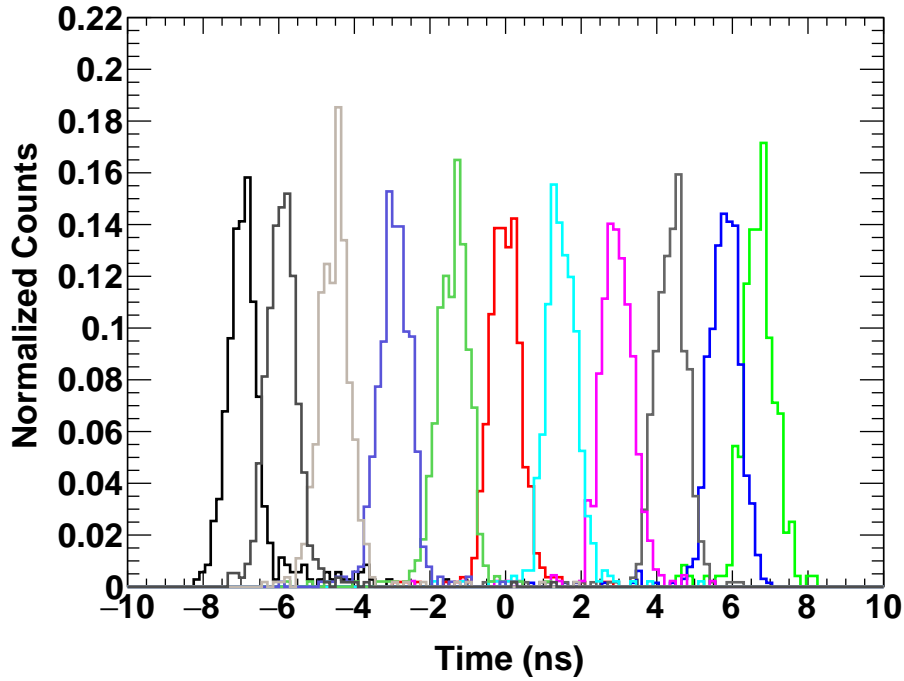


Figure 6. The measured time for muon events at 11 different positions shown for one of the detectors. The positions in cm are (-48.0, -40.1, -30.1, -20.1, -10.0, 0.0, 10.0, 20.1, 30.2, 40.3, 48.0).

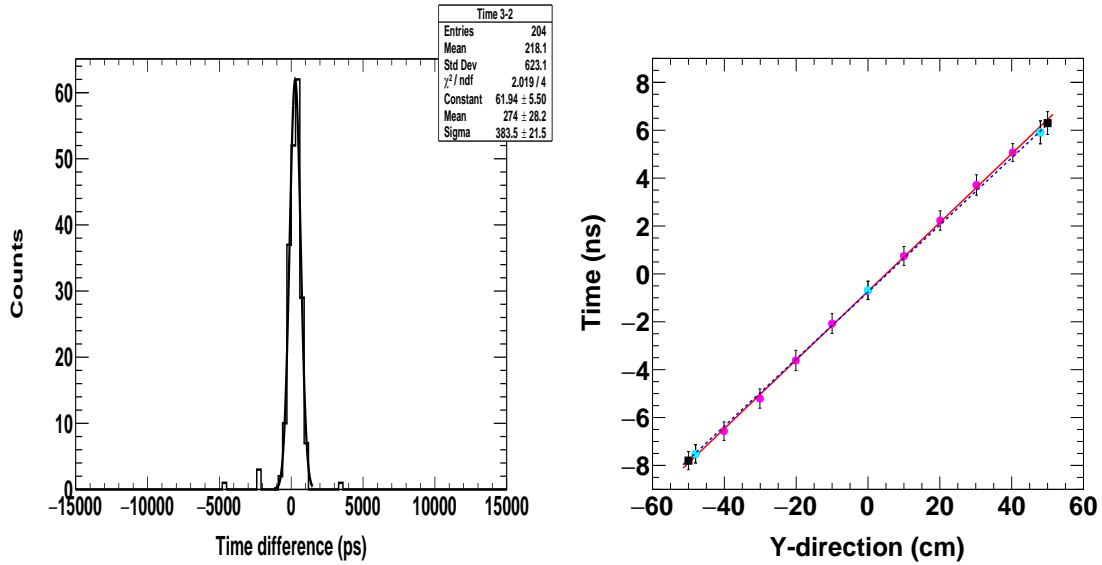


Figure 7. (a) Left: Time resolution obtained using vertical muons at center of detector 1 using Cross geometry G_{Cross} . (b) Right: The measured time difference plotted as a function of position of muon in scintillator bar at 11 positions. The solid line is a fit to 11 points and dashed line is a fit to three points (middle point and 2 last points) shown by blue. Two square black points at ± 50 cm are the points where the time difference distributions between two ends of the detector bar fall to 50% of their top value.

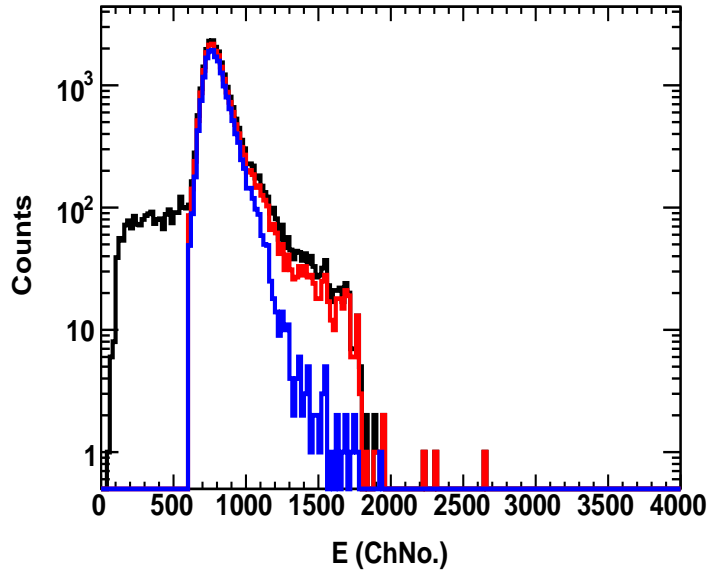


Figure 8. Geometric mean of the charge collection (in Channel number ChNo.) at the two ends of one of the detector in Square geometry G_{14} for Detector 2 (i) Black histogram corresponds to the coincidence of events within 7 ns with energy deposition > 0 ChNo. in all 4 detectors. (ii) Red histogram is the coincidence of events within 7 ns and with minimum energy deposition $E > 600$ ChNo. in all 4 detectors and (iii) Blue histogram is the coincidence of events within 7 ns and with minimum energy deposition $E > 600$ ChNo. in all 4 detectors and after cleaning muon events using track quality cuts defined later in the next subsections.

row shows inter detector time offset with respect to top detector (Det₃). The inter detector time offset is the time duration of the events between two detectors is also measured using vertical muons assuming them traveling with speed of light. The events are in coincidence when all the 8 signals from the four bars arrive within 25 ns. After all the corrections are done we are in a position to tighten the coincidence condition to have a time difference within 7 ns (5 ns in case of Close geometries G_{15} and G_{16}) in the top and bottom detector.

Table 4. Time correction for the center of each detector. The second line shows the inter detector timing offset with respect to top detector (Det₃).

Time (ps)	Det ₀	Det ₁	Det ₂	Det ₃
T_{center}	1194.0	-931.0	-37.0	-689.0
T_{offset}	1167.3	681.8	-340.4	0.0

3.2 Energy deposition

To construct the energy deposition E of the signal we take geometric mean of the two integrated charges E_1 and E_2 obtained at the two ends of the bars as $E = \sqrt{E_1 E_2}$. Since there is attenuation of the signal as it travels in the scintillator, the charge at the end where the event is closer will be more than that at the other end. Geometric mean makes the signal position independent. Signal gains are matched offline in all four detectors. Figure 8 shows

the geometric mean of the charge collection at the two ends of one of the detectors in the Square geometry G_{14} for Detector 2. Here, (i) Black histogram corresponds to the coincidence of events within 7 ns with energy deposition >0 ChNo. in all 4 detectors. (ii) Red histogram is the coincidence of events within 7 ns and with minimum energy deposition $E > 600$ ChNo. in all 4 detectors and (iii) Blue histogram is the coincidence of events within 7 ns and with minimum energy deposition $E > 600$ ChNo. in all 4 detectors and after cleaning muon events using track quality cuts defined later in the next subsections.

In the analysis, $E > 600$ ChNo. cut is placed on energy deposition where we see a step in the black histogram showing the starting of muon peak. The value of this cut is obtained such that very small number of muon events are lost, the method is presented in the next section. The energy calibration to convert channel number (ChNo.) with the energy in MeV is done after the tracking schemes are finalized in the next subsections.

Energy deposition is measured using Cross geometry G_{Cross} (for vertical muons) of detectors. The energy deposition by muons in each detector is fitted using the Langau (Landau+Gaussian) function. The ratios of Most Probable Value (MPV) for a detector and detector 0 is the energy gains of that detector with respect to detector 0. The energy deposition gain matching with respect to detector 0 are 1.11, 1.10 and 1.04 for detectors 1, 2 and 3 respectively. Table 5 shows the parameters of Langau (Landu+Gaussian) distribution function which was obtained by fitting energy deposition distribution with all final cuts in the detector 0 by vertical muons measured using Cross geometry G_{Cross} . This distribution of deposited energy is used as input in the simulation and these parameters are also used in the energy calibration.

Table 5. Langau parameters obtained by fitting energy deposition in the detector 0 by vertical muons measured using Cross geometry G_{Cross} .

Detector	Width	MPV	Area	GSigma
0	31.9	746.8	9256.3	32.2

3.3 Pulse Shape Discrimination (PSD)

Liquid scintillator has different pulse shapes of energy deposition for different particles which gives a unique handle of Pulse Shape Discrimination (PSD) as compared to other detectors. PSD parameter is defined as the ratio of difference of energy depositions by a particle in the detector in the Long gate (200 ns) and Short gate to the energy deposition by particle in Long gate as

$$\text{PSD} = \frac{E_{\text{Long}} - E_{\text{Short}}}{E_{\text{Long}}}. \quad (3.1)$$

Figure 9 shows 2D histograms of PSD versus energy for Detector 1 which is run in singles mode (a) Without AmBe source showing background particles and muon bump (b) With AmBe source showing neutrons and photons imposed over background and muons. Both the spectra are built over same acquisition time of ~ 13 minutes. One can clearly see that the neutrons have higher PSD as compared to photons. A lower threshold on energy cut on all 4 scintillators gives a clean muon spectrum. We also apply a PSD cut which removes heavy particles if any. The finalized PSD cuts obtained from this figure are $\text{PSD} < 0.6$ for G_{15} , G_{16}

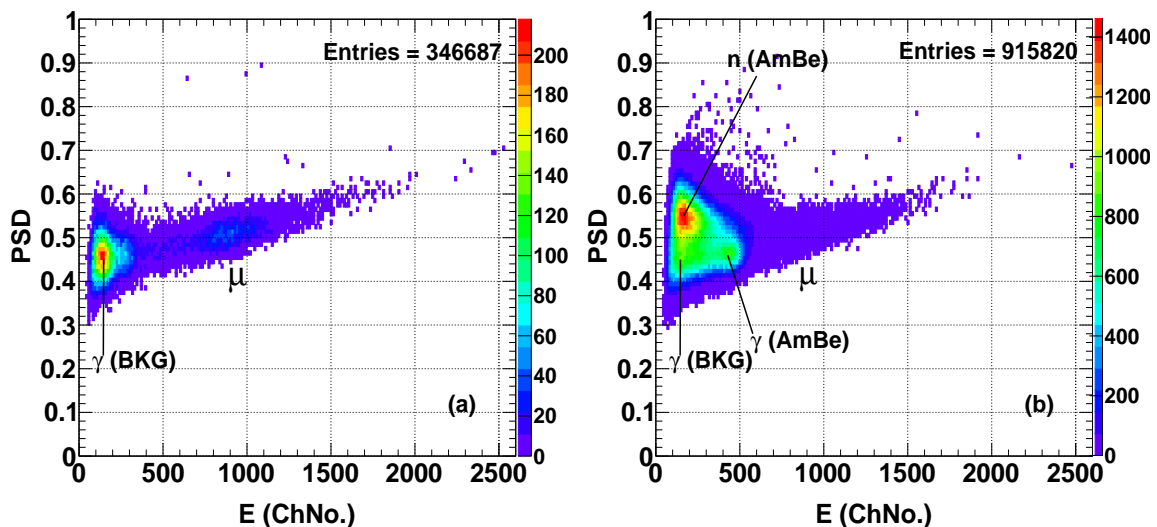


Figure 9. 2D histograms of PSD versus energy for Detector 1 which is run in singles mode (a) Without AmBe source showing background particles and muon bump (b) With AmBe source showing neutrons and photons imposed over background and muons. Both the spectra are built over same acquisition time of ~ 13 minutes.

and G_{17} where the Short gate value is 24 ns. Similar PSD < 0.78 is determined for all other geometries where the Short gate value is 20 ns.

3.4 Track quality parameters

In this analysis, we devise three dimensionless track quality parameters to reject the background events in m detectors. One is the usual χ^2/NDF . The other two are devised such that they favour tracks that take similar time to travel equal inter detector distances and deposit similar energy in all detectors.

1. χ^2/NDF : This is calculated by fitting a straight line to the m measured data points in m detectors.
2. Δt_{rms} : If t_0, t_1, t_2 and t_3 are the timings of events in the detectors starting from top to bottom then

$$\Delta t_{rms} = \sqrt{\frac{1}{m-1} \sum_{i=1}^{m-1} \left(\frac{\Delta t_i - \overline{\Delta t}}{\Delta t_i} \right)^2}, \quad (3.2)$$

$$\text{where } \Delta t_i = \frac{t_i - t_{i-1}}{(t_i - t_{i-1})_{\text{expected}}} \quad (3.3)$$

$$\text{and } \overline{\Delta t} = \frac{1}{m-1} \sum_{i=1}^{m-1} \Delta t_i. \quad (3.4)$$

Here $(t_i - t_{i-1})_{\text{expected}}$ is the time taken by the light from $(i-1)^{th}$ to i^{th} detector in downward sequence.

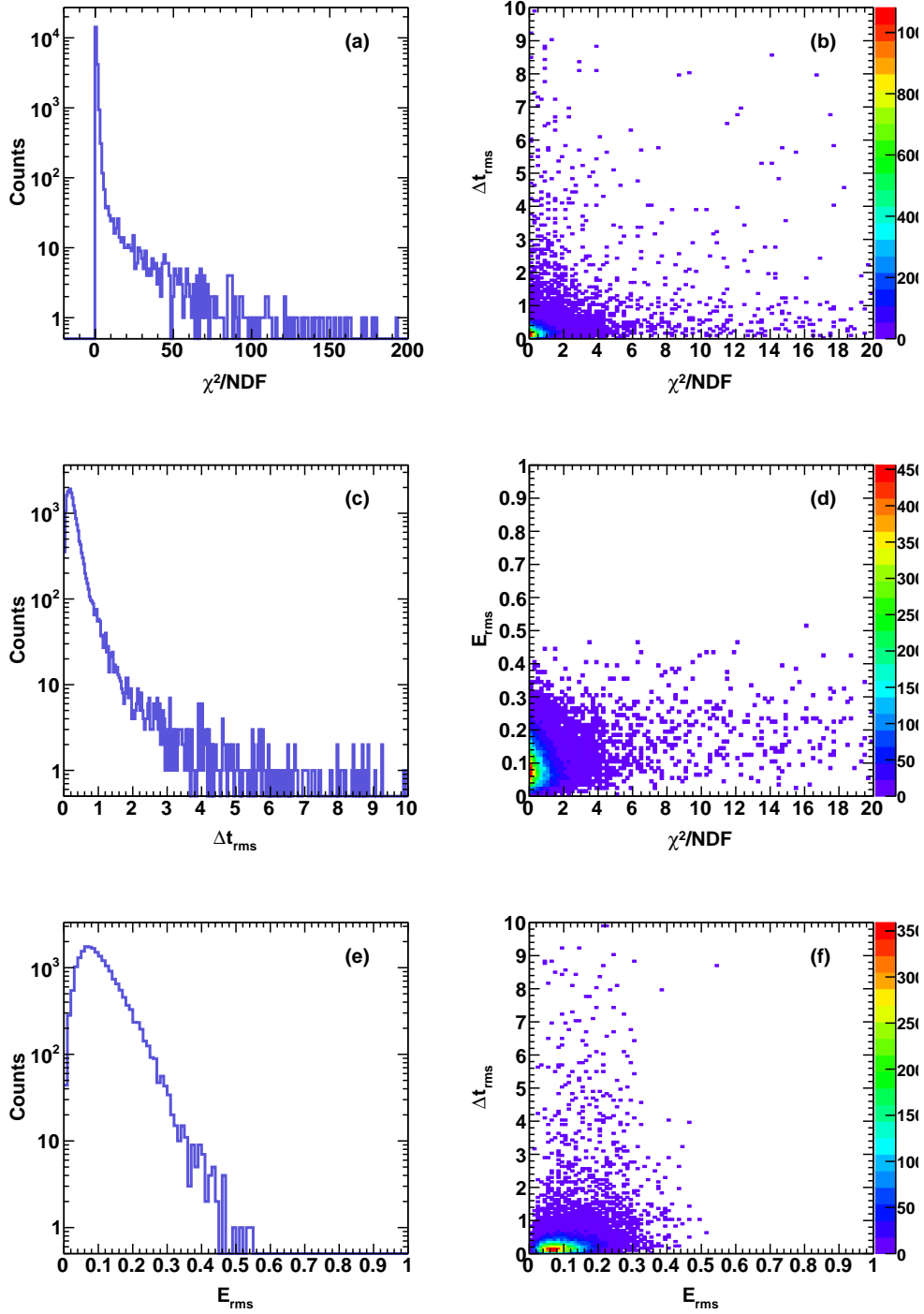


Figure 10. Distributions of track quality parameters and their correlations, for all the coincident events (within 7 ns) in the detectors with finalised cut on energy deposition and PSD in the Square geometry G_{14} , (a) χ^2/NDF (b) χ^2/NDF with Δt_{rms} (c) Δt_{rms} (d) χ^2/NDF with E_{rms} (e) E_{rms} and (f) Δt_{rms} with E_{rms} . It is clear from the correlation histograms (b), (d) and (f) that the track quality parameters are independent from each other and background can be reduced by applying cuts on each of the parameters.

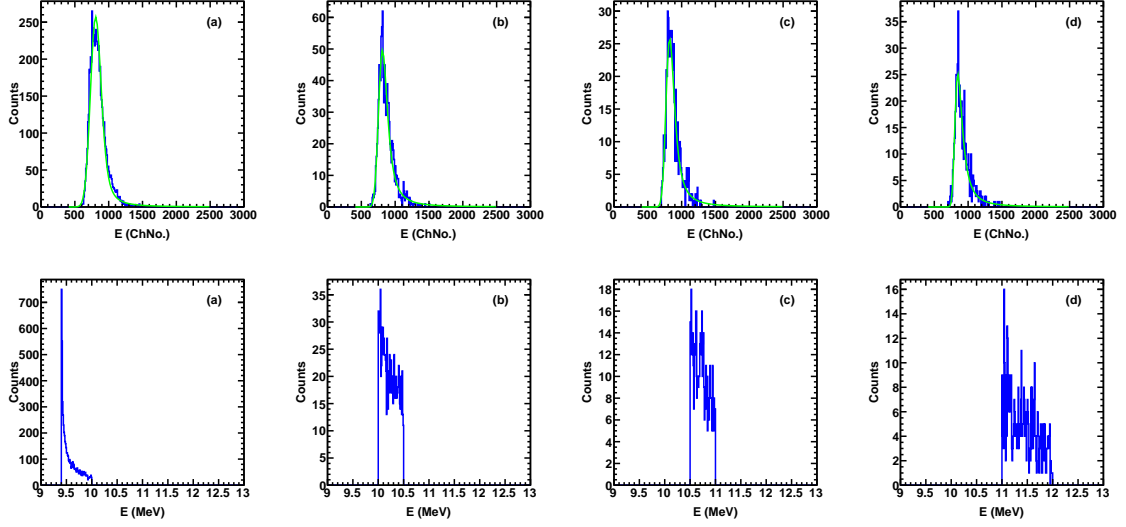


Figure 11. The energy spectra in channel number (top panels) in different bins of energy (lower panels) calculated using measured pathlengths traversed by muons in the detector. The energy bins used are 9.4-10 MeV, 10-10.5 MeV, 10.5-11 MeV and 11-12 MeV in the Square geometry G_{14} . Events are under finalised cut conditions as mentioned in the next section.

3. E_{rms} : If E_0 , E_1 , E_2 and E_3 are the energy depositions of events in the detectors 0, 1, 2 and 3 respectively then

$$E_{rms} = \sqrt{\frac{1}{m} \sum_{i=0}^{m-1} \left(\frac{E_i - \bar{E}}{E_i} \right)^2}, \quad (3.5)$$

$$\text{where } \bar{E} = \frac{1}{m} \sum_{i=0}^{m-1} E_i. \quad (3.6)$$

Figure 10 shows the distributions of track quality parameters and their correlations, for all the coincident events (within 7 ns) in the detectors with finalised cut on energy deposition and PSD in the Square geometry G_{14} , (a) χ^2/NDF (b) χ^2/NDF with Δt_{rms} (c) Δt_{rms} (d) χ^2/NDF with E_{rms} (e) E_{rms} and (f) Δt_{rms} with E_{rms} . It is clear from the correlation histograms (b), (d) and (f) that the track quality parameters are independent from each other and background can be reduced by applying cuts on each of the parameters.

3.5 Energy calibration

The detector width (active material) is 4.9 cm and thus energy loss expected for a vertical muon in the detector bar is $E_{\text{Vertical}} = 9.4$ MeV considering an energy loss of 1.92 MeV/cm for a muon of energy 2 GeV. Since we can reconstruct angle (θ) of the track and hence path lengths in a detector and thus we can calculate the energy depositions in MeV for a track at angle θ as

$$E(\theta) = \frac{E_{\text{Vertical}}}{\cos \theta} \quad (3.7)$$

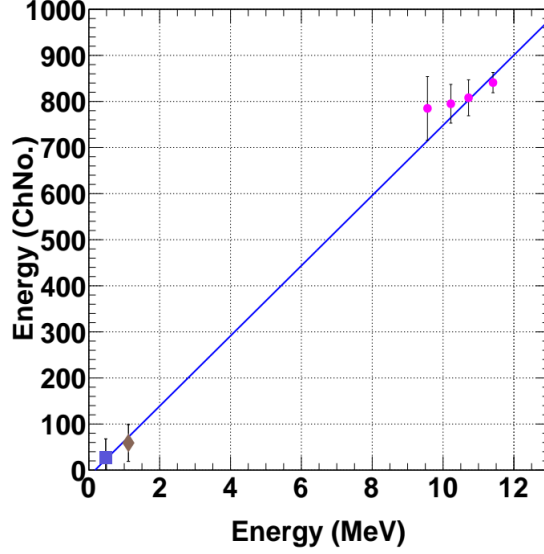


Figure 12. The peak channel number (MPV) of the energy spectra plotted as a function of mean energy in MeV calculated for each bin obtained using measured pathlength in the detector corresponding to tracks with different angles. The two lowest points are from the Compton edge of γ -ray from ^{137}Cs source (0.662 MeV) and ^{60}Co (1.332 MeV).

This allows us to fill energy spectrum in channel numbers in the required bins of energy in MeV as per Eq (3.7) constrained using pathlengths (measured using zenith angle of track). The channel number then can be calibrated in terms of energy. Figure 11 shows the energy spectra in channel number (top panels) in different bins of energy (lower panels) obtained using measured pathlengths traversed by muons in the detector. The events are under finalised cut conditions as mentioned in the next section. The energy bins used are 9.4-10 MeV, 10-10.5 MeV, 10.5-11 MeV, 11-12 MeV. The energy spectra in each bin are fitted with a Langau function and MPV is obtained. Figure 12 shows the peak channel number (MPV) of the energy spectra plotted as a function of mean energy in MeV calculated for each bin obtained using measured pathlength in the detector corresponding to tracks with different angles. The two lowest points are from the Compton edge of γ -ray from ^{137}Cs source (0.662 MeV) and ^{60}Co (1.332 MeV). The straight line is fitted including all points is given by

$$E_{\text{Ch}} = m \times E_{\text{MeV}} + c, \quad (3.8)$$

where $m = 76 \text{ ChNo./MeV}$ and $c = -13 \text{ ChNo.}$ Now we can calculate the energy cut in our analysis in MeV. Thus 600 ChNo., 720 ChNo. and 1600 ChNo. are equal to 8.07 MeV, 9.64 MeV and 21.22 MeV respectively.

4 Measurement of efficiencies

We obtain the efficiency of one of the middle detectors by using coincidence with the other 3 detectors with stringent cuts on energy deposition, PSD and track quality cuts. In the energy deposition range $E_{\text{cut}} < E < 1600 \text{ ChNo.}$ (including PSD), the efficiency of E_{cut} of detector

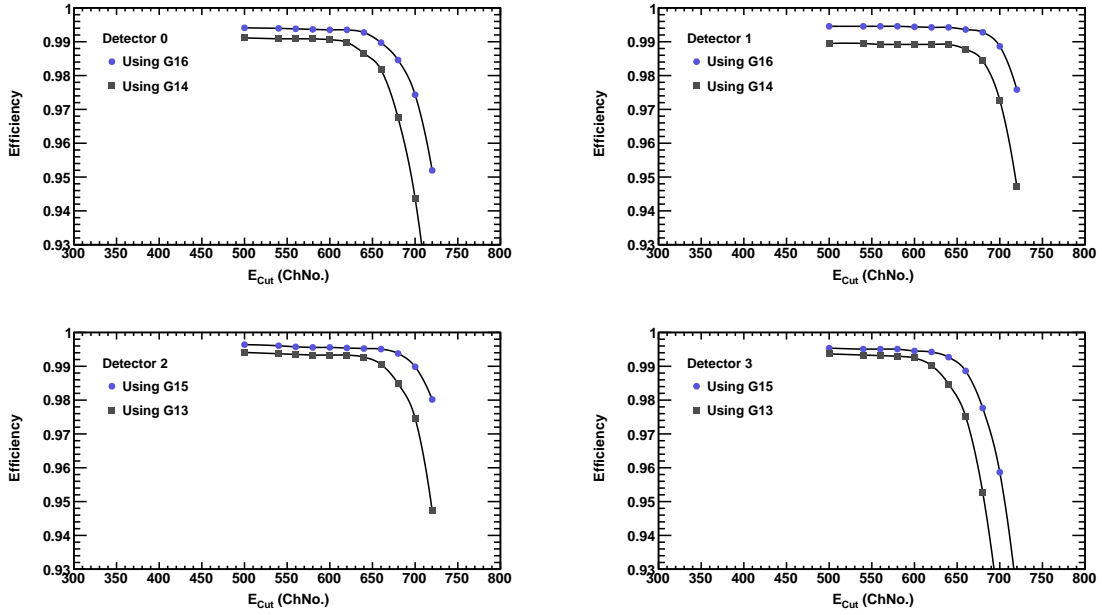


Figure 13. Efficiencies of detectors as a function of energy deposition for all 4 detectors using Close geometry G_{15} and G_{16} and Square geometries G_{13} and G_{14} . Here the cut is applied as $E_{Cut} < E < 1600$ ChNo.

1 in Close geometry G_{16} is calculated as

$$\epsilon_{E1} = \frac{\text{Counts in } (0 \times 1 \times 2 \times 3)}{\text{Counts in } (0 \times 2 \times 3)} \quad (4.1)$$

where stringent cuts are applied on other 3 detectors (0,2,3) to have incident muons which are background free. The values of stringent cuts on energy deposition, PSD and Track quality cuts are $720 \text{ ChNo.} < E < 1600 \text{ ChNo.}$, $\text{PSD} < 0.6$ (< 0.78 for Square and Large geometries), $\chi^2/\text{NDF} < 0.3$, $\Delta t < 0.3$ and $E_{rms} < 0.12$ respectively. This way efficiencies of two detectors 0 and 1 can be obtained in Close geometry G_{16} where they are placed in the middle. The geometry G_{15} (reverse of G_{16}) has been used to obtain efficiencies of detectors 2 and 3. In both the geometries G_{15} and G_{16} , the detectors were placed with a nominal separation of 3.2 cm among them to have an excellent alignment of all four bars. Later we also measure the efficiencies of middle detectors in Square geometries G_{13} and G_{14} . The efficiencies come down which now include the misalignment among the four detectors. The efficiencies of top and bottom detectors are taken from Close geometries G_{15} and G_{16} but the efficiencies of middle detectors are always taken from actual geometry of measurement. This includes the effect of possible misalignment for geometries where the inter detector distances are large.

Figure 13 shows the efficiencies of detectors as a function of energy deposition cuts E_{cut} in $E_{cut} < E < 1600$ ChNo.. Efficiencies of detectors for various energy deposition cuts were obtained using geometries G_{15} , G_{16} , G_{13} and G_{14} . With the help of this graph, we have chosen the finalised value of energy cut E_{cut} equal to 600 ChNo. (8.07 MeV) to reduce the background by signal ratio without compromising much on genuine muon events.

To measure the efficiency of track quality parameters we use a data driven method. Here to get the efficiency of the cut on a parameter under study, the other parameters and energy deposition cuts were kept stringent.

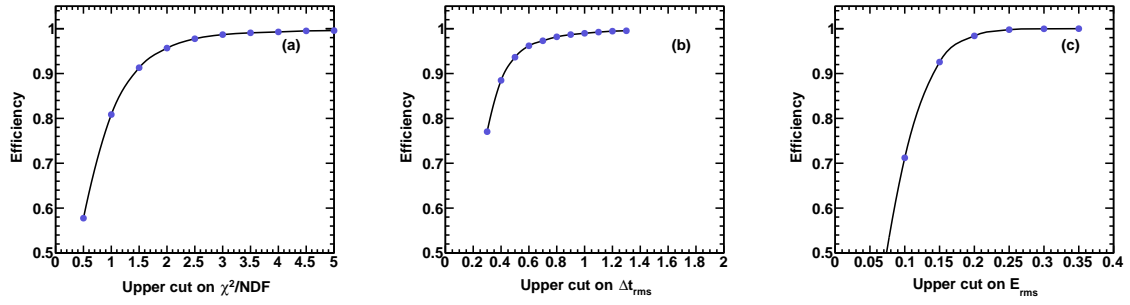


Figure 14. Efficiencies of track quality parameters as a function of the cuts for Square geometry G_{14} (a) Upper cut on χ^2/NDF (b) Upper cut on Δt_{rms} and (c) Upper cut on E_{rms} .

Figure 14 shows the efficiencies of track quality parameters as a function of the cuts for Square geometry G_{14} (a) Upper cut on χ^2/NDF (b) Upper cut on Δt_{rms} and (c) Upper cut on E_{rms} . With the help of these graphs we choose the values of tightest cuts but still be close to plateau region in order to keep the efficiency high. We have chosen the finalised values of tracking cuts $\chi^2/\text{NDF} < 3$, $\Delta t_{rms} < 0.9$ and $E_{rms} < 0.2$ for Square geometry G_{14} . For geometries G_{13} , G_{14-2} , G_{14-3} and G_{11} , the values of tracking cuts are kept same as those for G_{14} . The finalised values of tracking cuts for Small geometry G_{17} are chosen as $\chi^2/\text{NDF} < 3$, $\Delta t_{rms} < 2.5$ and $E_{rms} < 0.2$. The finalised value of tracking cuts for Close geometries (G_{15} and G_{16}) are chosen as $\chi^2/\text{NDF} < 3$, $\Delta t_{rms} < 2.5$ and $E_{rms} < 0.22$. In Small and Close geometries it was required to loosen the Δt_{rms} cut because of limited time resolution of the detectors.

Table 6. Efficiency of detectors in various geometries for muon detection at finalised energy deposition above $E_{\text{cut}} = 8.07$ MeV (including PSD cut).

Geometry	Det ₀	Det ₁	Det ₂	Det ₃
G_{14}	0.991 ± 0.001	0.989 ± 0.002	0.996 ± 0.001	0.994 ± 0.001
G_{13}	0.993 ± 0.001	0.994 ± 0.001	0.993 ± 0.001	0.992 ± 0.001
$G_{15} \& G_{16}$	0.993 ± 0.001	0.994 ± 0.001	0.996 ± 0.001	0.994 ± 0.001

Table 6 shows the efficiency of detectors in various geometries for muon detection at finalised energy deposition above $E_{\text{cut}} = 8.07$ MeV (including PSD cut) using Eq 4.1.

Table 7 shows efficiency of finalised tracking cuts for various geometries. Efficiency errors in Tables 6 and 7 are calculated using binomial error $\sigma_\epsilon = \sqrt{\epsilon(1-\epsilon)/N}$, where N is the total number of incident events and ϵ is the efficiency of the optimised cut.

5 Monte Carlo simulation and geometrical acceptance

To obtain the accepted muon distribution in the detector setup, Monte Carlo simulations are performed. The muon events ($N_m = 7000000$) are uniformly generated at the lower face of top detector using Monte Carlo generator uniformly in ϕ and as per θ given by

$$I(\theta) = I_0 \cos^n \theta \quad (5.1)$$

Table 7. Efficiency of finalised tracking cuts for various geometries.

Geometry	ϵ_1 (χ^2/NDF)	ϵ_2 (Δt_{rms})	ϵ_3 (E_{rms})
G_{13}	0.986 ± 0.001	0.989 ± 0.001	0.987 ± 0.002
G_{14}	0.987 ± 0.001	0.987 ± 0.002	0.984 ± 0.002
G_{11}	0.985 ± 0.002	0.986 ± 0.002	0.986 ± 0.002
G_{17}	0.992 ± 0.001	0.971 ± 0.002	0.986 ± 0.002
G_{14-2}	0.971 ± 0.002	0.994 ± 0.001	0.980 ± 0.002
G_{14-3}	0.974 ± 0.002	0.988 ± 0.002	0.977 ± 0.002
G_{15}	0.984 ± 0.001	0.992 ± 0.001	0.987 ± 0.002
G_{16}	0.987 ± 0.001	0.983 ± 0.001	0.984 ± 0.002

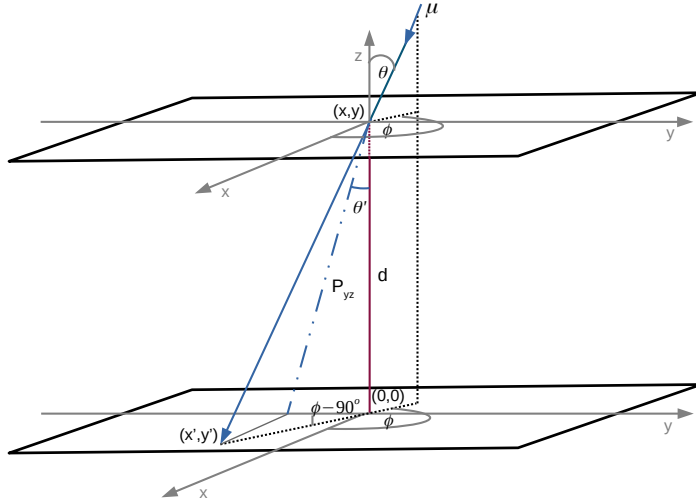


Figure 15. Picture used for the first estimate of acceptance using lower plane of top detector and top plane of bottom detector.

The value of exponent $n \sim 2.1$ is obtained by fitting the simulated and accepted distribution with the experimentally measured distribution. We also generate energy deposition in each scintillator using the measured energy shape for vertical muons using Langau function (parameters are given in Table 5). These energy depositions are scaled as per the pathlengths decided by the position of event and the generated angles θ and ϕ . Figure 15 shows the picture used for the first estimate of acceptance using lower plane of top detector and top plane of bottom detector separated by a distance d . Let us define that the z-axis is perpendicular to the plane of the detectors and the x- and y-axis lie in the horizontal plane of the detectors. Now assume that a muon traveling at a certain zenith angle θ and an azimuthal angle ϕ hits the top detector bar at the coordinates (x, y) , then it travels and hits the bottom bar at position (x', y') which can be calculated as

$$(x', y') = (x - d \tan \theta \cos \phi, y - d \tan \theta \sin \phi). \quad (5.2)$$

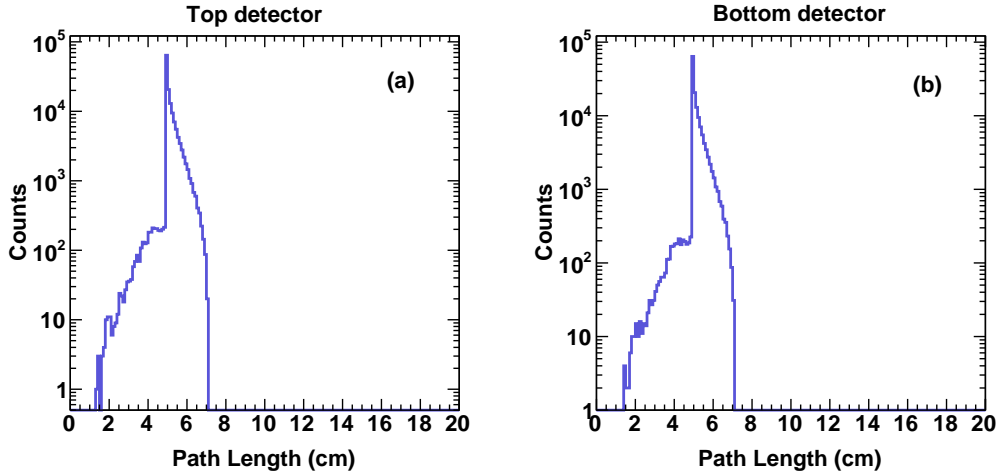


Figure 16. The distributions of pathlength traversed by the accepted muons in the (a) Top and (b) Bottom detectors for energy deposition above 8.07 MeV in the Square geometry G_{14} .

If the point (x', y') falls within the area of the lower detector it is considered in the next step. Out of these selected events, only those muons are accepted which travel pathlengths to have minimum energy deposition (corresponding to the energy cut) in both top and bottom detectors. This way we get an accepted θ distribution in the detector. Since we measure θ only in 2 dimensions (yz plane) but having a finite ϕ coverage, the measured θ' (ϕ corrected) will be given by

$$\theta' = \cos^{-1} \left(\frac{d}{P_{yz}} \right) \quad (5.3)$$

where P_{yz} is the projected track length on the yz plane.

Figure 16 shows the distributions of pathlength traversed by the accepted muons in the (a) Top and (b) Bottom detectors for energy deposition above 8.07 MeV in the Square G_{14} geometry. It is clear from both figures that for energy deposition less than 8.07 MeV, muons with smaller pathlength will be rejected, such muons actually pass through the side faces of the detectors.

Figure 17(a) shows the generated zenith angle distribution on the top detector using $n = 1.86$ and total events = 7000000 normalized to $I_o = 65.38/m^2/sr/s$. Figure 17(b) shows the Accepted θ distribution. Figure 17(c) shows the Accepted θ distribution (ϕ corrected) as mentioned in Eq. 5.3. Figure 17(d) shows the acceptance which is the accepted/generated (counts in (b)/counts in (a)) in the Square geometry G_{14} after muon minimum energy deposition 8.07 MeV in the top and bottom detectors.

The acceptance α is then obtained by ratio of such accepted events to the generated events as

$$\alpha = \frac{\text{Accepted events}}{\text{Generated events}} \quad (5.4)$$

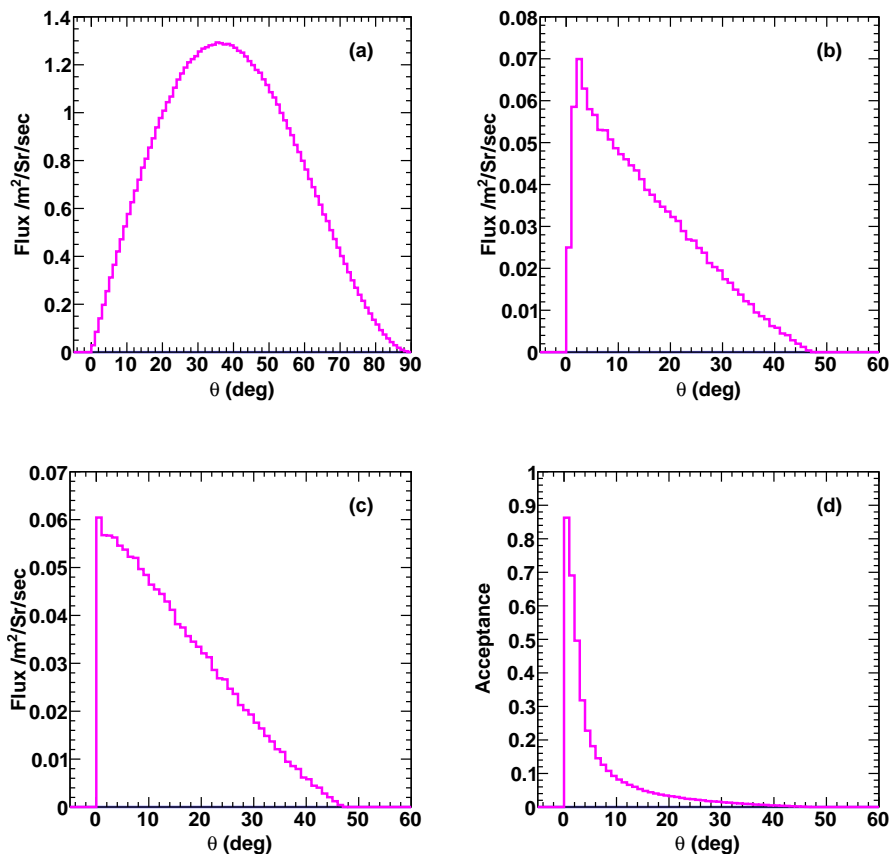


Figure 17. (a) The generated zenith angle θ distribution on the top detector using $n = 1.86$ and normalized to $I_o = 65.38/m^2/sr/s$. (b) Accepted θ distribution (c) Accepted θ distribution (ϕ corrected). (d) Acceptance α which is Accepted/Generated, in the Square geometry G_{14} .

6 Muon flux measurements using different geometries

In this section, we present the muon flux measurements using the geometries given in section 2. Our most optimized geometries are the Square geometries G_{14} and G_{13} . These are called Square geometries since the distance between top and bottom detectors is about 95 cm giving a shape of Square looking from a side (yz plane). The inter detector distances are kept almost equal and are nearly 3 times larger than the distances corresponding to time resolution of the detectors. This allows inter detector timings to be used to decide track quality. Our setup is capable of distinguishing between upgoing track and downgoing tracks. The position resolution involving 4 bars is 1.5 cm. The track angle resolution for this geometry is 1 degree for higher angles which increases to 2 degrees for small angles.

Figure 18 shows the time taken by a muon track starting from top detector (3) in the Square geometry G_{14} for (a) Detector 3 (b) Detector 1 (c) Detector 0 and (d) Detector 2. The distances of the three detectors from the top detector corresponds to 31.7 cm, 63.2 cm and 95.0 cm. Green histogram is for muon events in all 4 detectors with final cuts and blue histogram is for vertical muon events (tolerance is $\pm 5^\circ$) in all 4 detectors with final cuts. This histogram is fitted with gaussian function. Green histogram is broader towards right side due

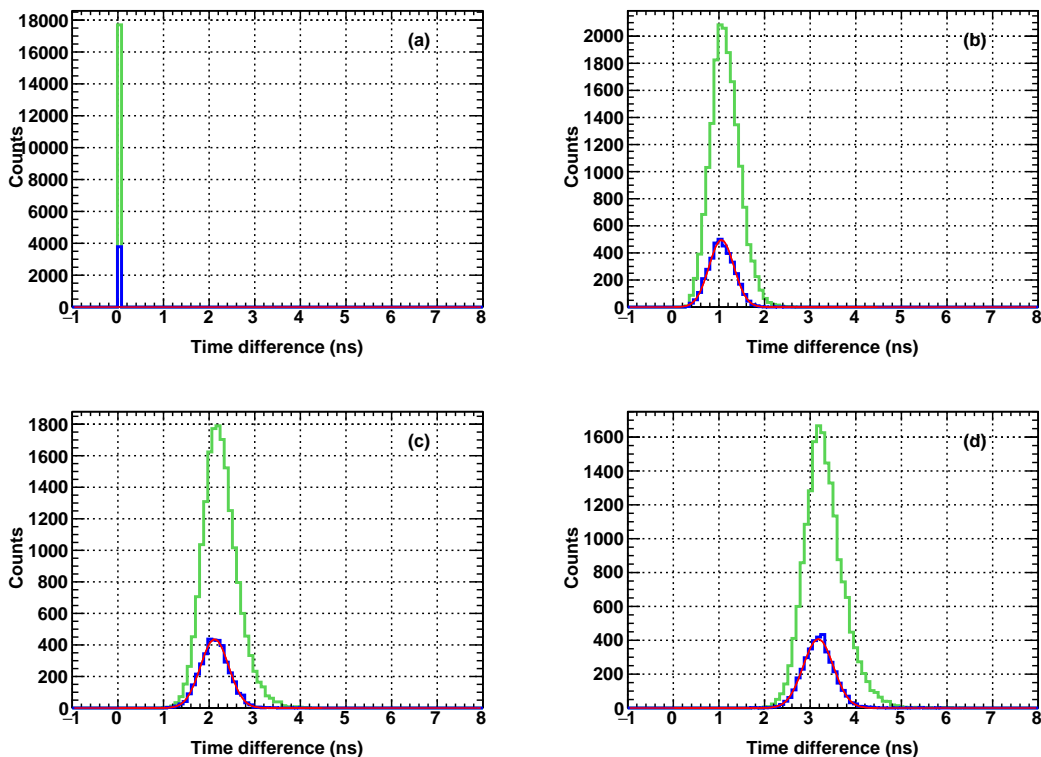


Figure 18. Time taken by a muon track starting from top detector (3) in the Square geometry G_{14} for (a) Detector 3 (b) Detector 1 (c) Detector 0 and (d) Detector 2. The distances of the three detectors from the top detector corresponds to 31.7 cm, 63.2 cm and 95.0 cm. Green histogram is for muon events in all 4 detectors with final cuts and blue histogram is for vertical muon events (tolerance is $\pm 5^\circ$) in all 4 detectors with final cuts. This histogram is fitted with gaussian function.

to tracks corresponding to larger zenith angles.

In the analysis, we can visualize the events track by track along with the track parameters. This has been very useful in devising the selections on various quality parameters. Figure 19 shows a muon track reconstructed in the Square geometry G_{14} along with quality parameters explained in the previous section. The timing values written towards the right side of the detector are the time (ns) taken by the muon track between the two detectors. The times in brackets are time taken by a light ray to traverse between the two detectors in same direction as the muon track. The value of energy deposited by the track in each detector is written towards left side of each detector.

We also use a Large Geometry G_{11} corresponding to an increased distance of the top detector from bottom. The Small Geometry G_{17} is a squeezed setup of four bars and the inter detector distances are kept equal. This geometry can cover zenith angles upto 60 degrees but with some increase in angular resolution. Figure 20 shows a muon track reconstructed along with the corresponding track quality parameters in the setups (a) Large G_{11} and (b) Small G_{17} .

Close geometries G_{15} and G_{16} are used to measure the efficiencies of the detectors where the inter detector separations are kept very small. The angular resolution of these geometries are very poor and thus will not give a good zenith angle distribution. Figure 21 shows the

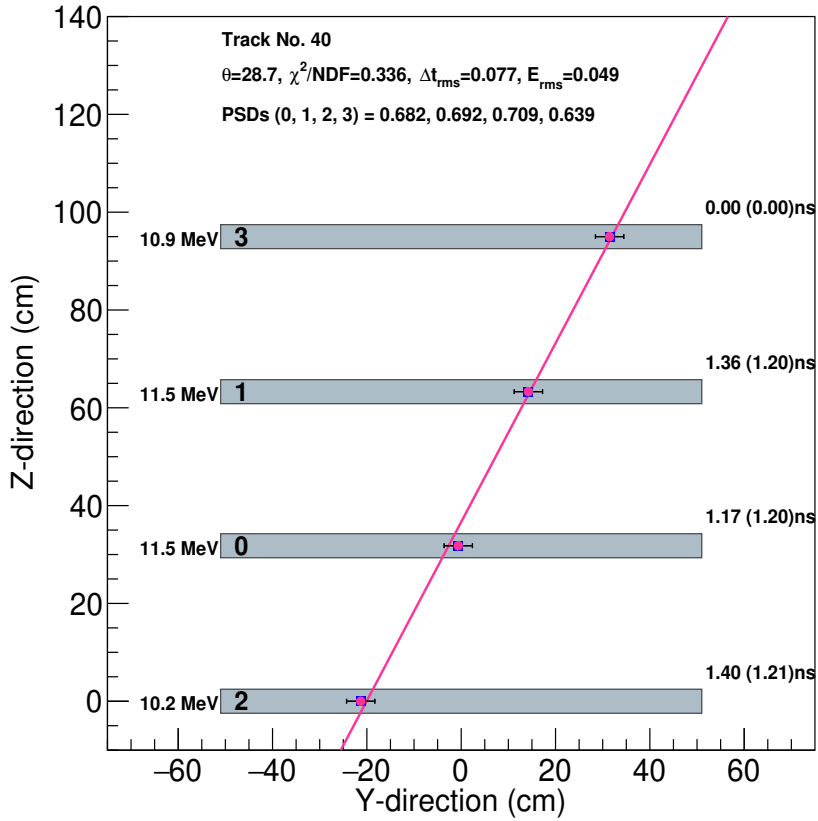


Figure 19. A muon track reconstructed in the Square geometry G_{14} along with quality parameters explained in the text. The timings written towards the right side of the detectors are the time taken by the muon track between the two detectors in nanoseconds. The time values in brackets are time taken by a light ray to traverse between the two detectors in the same direction as the track. The value of energy deposited in each detector is written towards the left side of each detector.

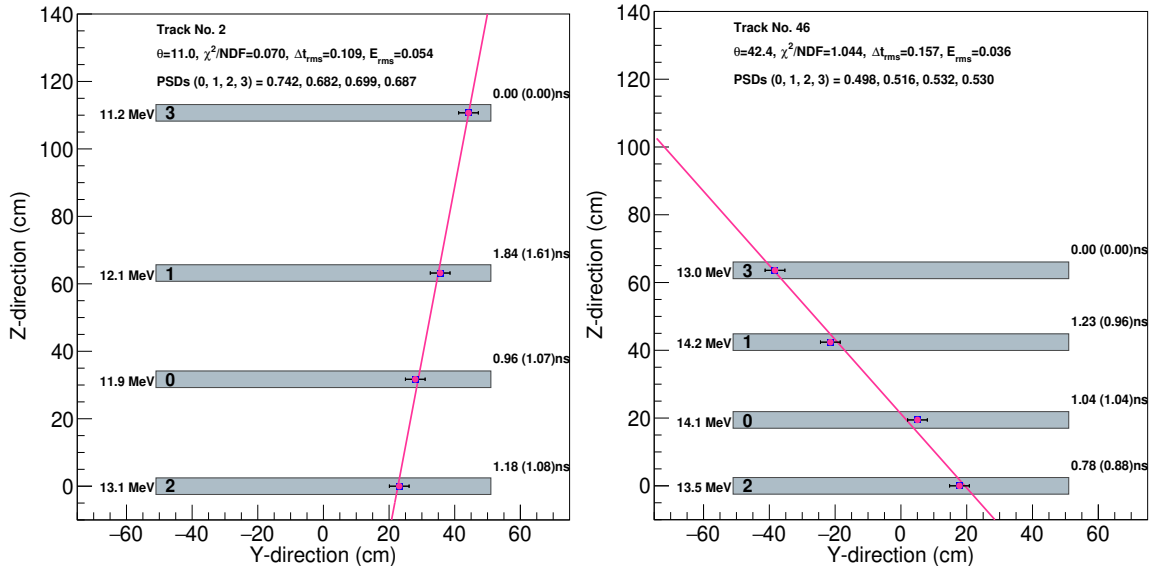


Figure 20. A muon track reconstructed in (a) Large G_{11} geometry and (b) Small G_{17} geometry along with the track quality parameters explained in the text.

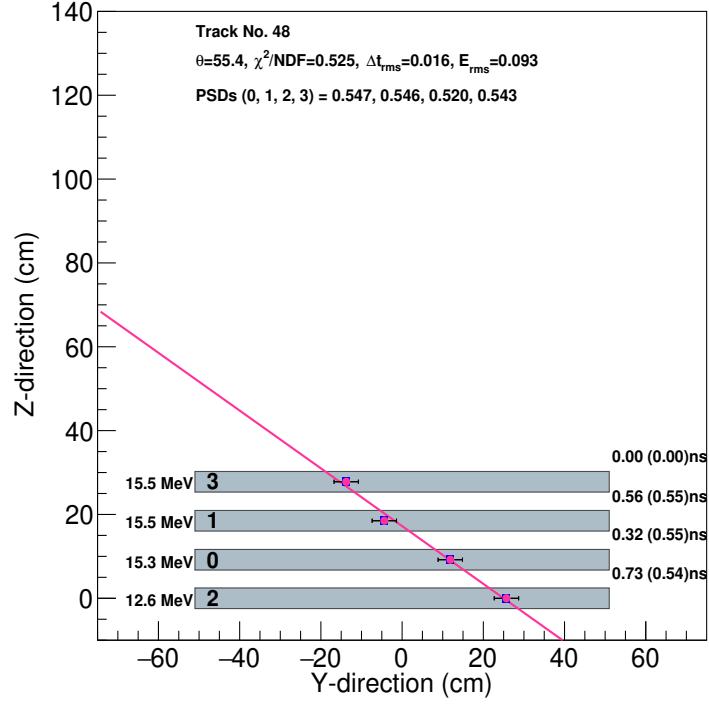


Figure 21. A muon track reconstructed in the Close geometry G_{16} along with the track quality parameters explained in the text.

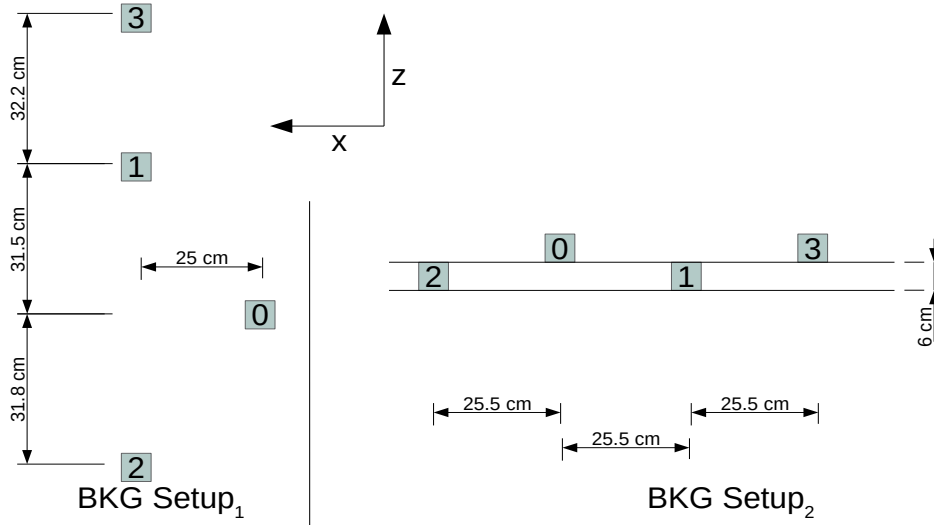


Figure 22. Setups used to measure the uncorrelated background.

muon track reconstructed in the Close geometry G_{16} along with the track quality parameters.

To measure the backgrounds we use two kinds of setups. One in which we shift one of the middle detectors in the Square geometry by a distance of 25 cm. In another setup, we place the detectors horizontally such that alternating detectors are shifted up by 6 cm. Figure 22 shows these two background setups.

The corrected flux distribution in the detector can be estimated from the observed muon counts as

$$I(\theta) = \frac{N_{\text{meas}}(\theta)}{A \times \epsilon \times \Omega \times t}, \quad (6.1)$$

where the $N_{\text{meas}}(\theta)$ is the number of events registered in the setup during data acquisition time t . Here, A is the area of top scintillator surface which is equal to $0.056 \times 1.02 \text{ m}^2$ and ϵ is the efficiency of setup is given by

$$\epsilon = \epsilon_E \times \epsilon_1 \times \epsilon_2 \times \epsilon_3, \quad (6.2)$$

where ϵ_E is the energy deposition and PSD cut efficiency of all the detectors, three or four used and $\epsilon_1, \epsilon_2, \epsilon_3$ are the efficiencies of the cuts of three track quality parameters. Here, Ω is the solid angle (which covers θ and ϕ from $0 - \pi/2$ and $0 - 2\pi$ respectively) given in terms of exponent n of the zenith angle distribution by

$$\Omega = \frac{2\pi}{n+1}. \quad (6.3)$$

For a given n , thus the flux is obtained by integrating $I(\theta)$ in Eq. 6.1 and divide by α . But in the detailed analysis, we fit I_0 and n using accepted simulated distribution as in Figure 17(c) on the measured distribution in Eq. 6.1. Note that n enters Eq. 6.1 through Ω .

Table 8 gives the comparison of events measured using 4/3 liquid scintillator bars in Square (G_{13}, G_{14}), Large (G_{11}), Small (G_{17}), and Close geometries (G_{15}, G_{16}) along with background setups. This table is made with keeping $n = 2$ fixed and demonstrates the comparison of effects of different cuts on different geometries. G_{14-2} and G_{14-3} are the setup of 3 detectors in which Det₂ and Det₃ are removed respectively from Square geometry G_{14} . Here distance in 2nd column corresponds to the distance between top and bottom detectors. We mention here that the acceptance for background setups corresponds to the distance in Square setup G_{14} although the distances in actual background setups (Figure 22) are smaller.

We define I_1, I_2, I_3, I_4 as the integrated muon fluxes (corrected with efficiencies and acceptance α using) under 4 finalised cuts conditions as described below.

1. I_1 : Particle gets detected in coincidence within 7 ns (5 ns) time in all 4 detectors and with finalised energy deposition E_{cut} and PSD cut.
2. I_2 : All track events with finalised χ^2/NDF cut on I_1 .
3. I_3 : All track events with finalised Δt_{rms} cut on I_2 .
4. I_4 : All track events with finalised E_{rms} cut on I_3 .

One can note from Table 8, the effectiveness of the tracking cuts by comparing the values of numbers corresponding to four fluxes. The values of I_4 for all geometries duly corrected for acceptance and efficiencies are consistent with each other shows robustness of our analysis method. The table also shows that the measurements with only 3 detectors are reasonably good if we use all the track quality cuts with the 3 bars. We also give two setups to measure uncorrelated backgrounds which shows that uncorrelated background is negligible for our measurements for both 4 and 3 detectors. The actual flux is obtained by fitting the measured zenith angle distribution with simulated distribution using I_0 and n as free parameters in the next section.

Table 8. The comparison of events measured from 4/3 liquid scintillator bars in Square (G_{13} , G_{14}), Large (G_{11}), Small (G_{17}), and Close geometries (G_{15} , G_{16}) along with background setups. I_1 , I_2 , I_3 , I_4 are the muon fluxes under the 4 cuts conditions as described in the text. Here $n = 2$ is fixed. Raw counts correspond to I_4 .

Geometry	Distance (cm)	Time (s)	Acceptance α	I_1 / $m^2/sr/s$	I_2 / $m^2/sr/s$	I_3 / $m^2/sr/s$	$I_4 \pm \text{Stat.}$ / $m^2/sr/s$	Counts
G_{14} (3,1,0,2)	95	113107	0.0213	73.02	69.95	68.15	66.02 ± 0.5	17703
G_{13} (1,3,2,0)	95	135733	0.0213	74.00	70.67	68.45	66.67 ± 0.45	21657
G_{11} (3,1,0,2)	110.7	104319	0.0167	74.27	71.09	69.47	67.20 ± 0.59	13030
G_{17} (3,1,0,2)	63.6	61495	0.0381	72.42	70.17	67.19	65.04 ± 0.5	16825
G_{14-2} (3,1,0)	63.2	113107	0.0384	75.01	71.18	69.41	66.21 ± 0.37	31726
G_{14-3} (1,0,2)	63.3	113107	0.0384	75.29	70.76	69.32	66.85 ± 0.37	31866
Efficiency Setups								
G_{15} (3,1,0,2)	27.8	25459	0.1043	68.78	67.5	66.69	65.08 ± 0.47	19539
G_{16} (3,1,0,2)	27.8	27169	0.1042	69.42	68.32	66.55	65.00 ± 0.45	20574
Background Setups								
BKG Setup1 (3,1,0,2)	95	16051	0.0213	1.64	0.15	0.05	0.05 ± 0.04	2
BKG Setup2 (3,1,0,2)	95	39149	0.0295	1.08	0.06	0.05	0.04 ± 0.02	4
BKG Setup2-2 (3,1,0)	63.2	39149	0.0384	2.24	0.60	0.37	0.25 ± 0.04	42
BKG Setup2-3 (1,0,2)	63.2	39149	0.0384	2.51	0.69	0.29	0.19 ± 0.03	31

7 Results with systematic uncertainties and discussions

As we have stated that the actual flux is obtained by fitting the measured zenith angle distribution with simulated distribution using I_0 and n as free parameters. In the following we give the measured zenith angle distributions along with simulated distributions for all setups with best fit values of I_0 and n given in Table 9.

Figure 23 shows the measured and simulated zenith angle distribution of cosmic muons in geometries (a) Square G_{13} , (b) Square G_{14} , (c) Large G_{11} , (d) Small G_{17} , (e) 3 Detectors G_{14-2} and (f) 3 Detectors G_{14-3} for best fit values of I_0 and n . Figure 24 shows the measured and simulated zenith angle distribution of cosmic muons in Close geometries (a) G_{15} and (b) G_{16} for fixed values of $I_0 = 66.70$ / $m^2/sr/s$ and $n = 2.1$. The simulation and observed distributions are not expected to have a good match for these geometries as the angular resolution becomes poor for smaller inter detector distances. The measurements presented in Figure 23 and Figure 24 include efficiencies of finalised cuts on energy deposition, PSD and tracking quality. The value of these cuts and their respective efficiencies are given in Table 6 and Table 7.

We use many geometries for obtaining systematic uncertainties as follows.

1. Setup-1: Flux from Square geometry G_{14} .
2. Setup-2: Flux from Square geometry G_{13} .
3. Setup-3: Flux from Large geometry G_{11} .
4. Setup-4: Flux from Small geometry G_{17} .

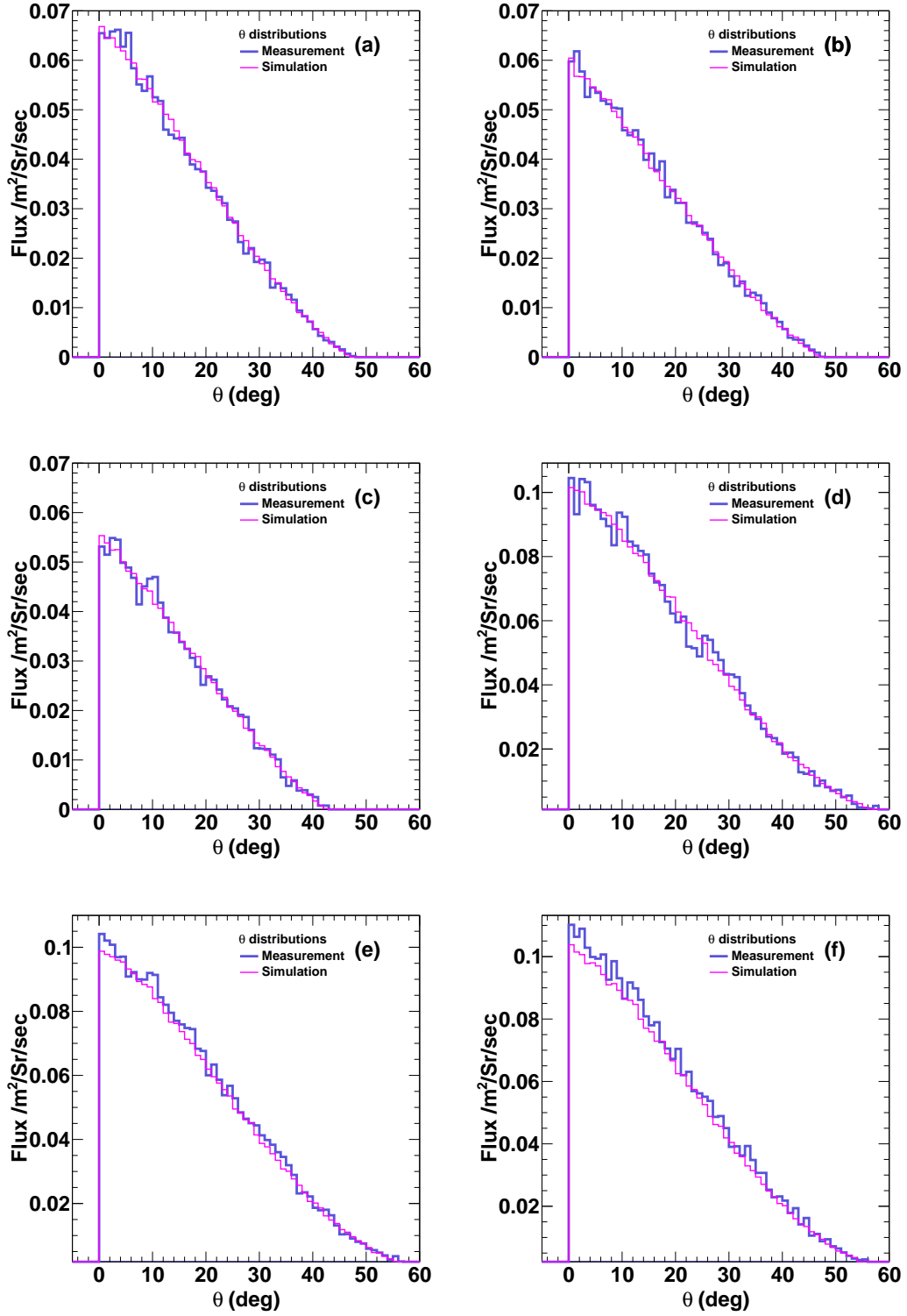


Figure 23. The measured and simulated zenith angle distribution of cosmic muons in geometries (a) Square G_{13} , (b) Square G_{14} , (c) Large G_{11} , (d) Small G_{17} (e) 3 Detector geometry G_{14-2} and (f) 3 Detector geometry G_{14-3} for best fit values of I_0 and n .

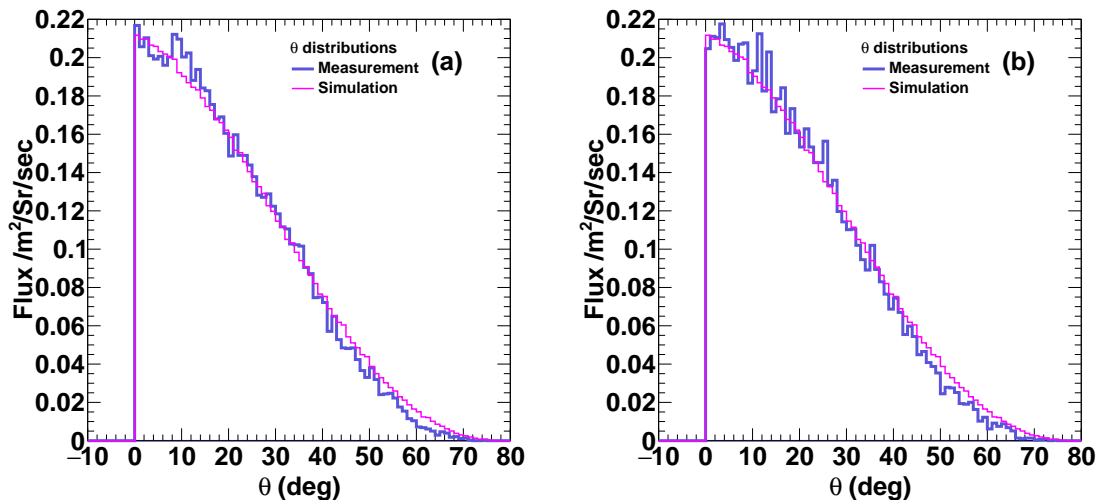


Figure 24. The measured and simulated zenith angle distribution of cosmic muons in Close geometries (a) G_{15} and (b) G_{16} for best fit values of I_0 and n

5. Setup-5: Flux from upper 3 detectors (3,1,0) in Square geometry G_{14-2} .
6. Setup-6: Flux from lower 3 detectors (1,0,2) in Square geometry G_{14-3} .
7. Setup-7: Flux from Square geometry G_{14-t} changing the time-position calibration.
8. Setup-8: Flux from Square geometry G_{13-t} changing the time-position calibration.
9. Setup-9: Flux from Square geometry G_{14A-} , with acceptance variation such that the distance between top to bottom detectors is decreased by 0.5 cm.
10. Setup-10: Flux from Square geometry G_{14A+} , with acceptance change such that the distance between top to bottom detectors is increased by 0.5 cm.

The above variations are carefully planned to cover all possible uncertainties affecting the measurements. The acceptance calculation and efficiency measurements are performed for each geometry separately. Varying the distances among the detectors covers most of the systematics like errors due to misalignments and separations among detectors affecting acceptance of the detector which is usually a major source of error. This also includes any variation coming from modeling the detector in the simulations. All the data has been taken during day time in the months of september, october and november 2021. The three geometries with different distances also include the variation of measurement dates. Interchanging detector positions include any bias due to any residual differences among the detectors affecting angle distribution. We also measure after removing one of the detectors to take into account any change due to the number of detectors involved. The time position relation affecting the value of n has been taken into account.

Table 9 shows the values of n and I_0 along with the fitting error from different setups. The averaging and systematic error calculations for flux and exponent for 10 Setups (N=20 including \pm error on fitting) are performed using the following equations.

$$I_{mean} = \frac{1}{N} \sum I_i, \quad (7.1)$$

$$\Delta I_{rms} = \sqrt{\frac{1}{N} \sum_{i=1}^N (I_i - I_{mean})^2}. \quad (7.2)$$

Combining all these measurements the vertical muon flux measured is $66.70 \pm 0.36(stat) \pm 1.50(sys) /m^2/sr/s$ with $n = 2.10 \pm 0.05(stat) \pm 0.25(sys)$ in $\cos^n \theta$.

The measurement was carried out inside a single floor building with rooftop. The muon momentum cutoff in our setup is calculated to be 255 MeV/c in simulation, which includes the standard rooftop over the setup with 15 cm concrete and 10 cm bricks.

Table 9. The values of I_0 and n for different measurements. All of them are used in calculating systematic error.

Setup	I_o ($/m^2/sr/s$) $I_o \pm \sigma(fit)$	n -value $n \pm \sigma(fit)$	χ^2/NDF (minimum)
1. Square G_{14}	65.375 ± 1.625	1.855 ± 0.125	0.910
2. Square G_{13}	67.250 ± 1.150	2.120 ± 0.090	1.012
3. Large G_{11}	66.875 ± 1.125	2.010 ± 0.200	1.395
4. Small G_{17}	66.125 ± 0.875	2.285 ± 0.075	1.258
5. G_{14-2}	67.650 ± 0.650	2.230 ± 0.100	1.071
6. G_{14-3}	68.300 ± 0.800	2.345 ± 0.085	1.058
7. Square G_{14-t}	67.125 ± 1.375	2.310 ± 0.100	1.070
8. Square G_{13-t}	67.250 ± 0.750	2.195 ± 0.165	1.119
9. Square G_{14A-}	65.030 ± 1.530	1.900 ± 0.260	0.956
10. Square G_{14A+}	66.000 ± 1.000	1.745 ± 0.135	0.979

Table 10 shows the comparison of vertical muon flux values measured by other experiments. In general, the value of vertical muon flux increases with increasing the geomagnetic latitude and altitudes although one can note from rows 2, 4 and 5 that there is large variation among the measurements made at similar conditions. Our value of muon flux is larger than the earlier measurement by Pal et al. [17]. One reason is that our momentum cutoff is slightly smaller. Although exact systematic error has not been estimated in their work, a later work using similar setup by the same group [16] gives a systematic error of 7.5% in flux measurement. The systematic error in our flux measurement is 2.2%. Thus, they are consistent within the errors and the present value is more accurate.

8 Summary and outlook

In this work, we report measurement of muon flux and angular distributions using different geometries of four one-meter long liquid scintillator bars. We exploit energy and excellent timing of scintillators to construct two dimensional tracks and hence angles of charged particles. Our analysis involves many innovative methods. Position calibration of scintillator bars is performed using vertical cosmic muons constrained by placing the four scintillators

Table 10. Comparison of vertical muon flux with other experiments.

References	Geomag. Lat. ($^{\circ}$ N)	P_c (GV)	Altitude (m)	P_{μ} (GeV/c)	n	Flux I_o ($m^{-2}s^{-1}sr^{-1}$)
Hayman et al. [5]	57.5	1.8	S.L.	≥ 0.320	-	76 ± 0.6
Greisen [6]	54	1.5	259	≥ 0.33	2.1	82 ± 1
Judge and Nash [7]	53	-	S.L.	≥ 0.7	1.96 ± 0.22	-
Crookes and Rastin [8]	53	2.2	40	≥ 0.35	2.16 ± 0.01	91.3 ± 0.2
Barbouti and Rastin [2]	52	2.5	40	≥ 0.438	-	88.68 ± 1.15
Fukui et al. [10]	24	12.6	S.L.	≥ 0.34	-	73.5 ± 2
Gokhale [2]	19	-	124	≥ 0.27	-	75.5 ± 1
Karmakar et al. [13]	16	15.0	122	≥ 0.353	2.2	89.9 ± 0.5
Sinha and Basu [14]	12	16.5	30	≥ 0.27	-	73 ± 2
Allkofer et al. [16]	9	14.1	S.L.	≥ 0.32	-	72.5 ± 1
Pethuraj et al. [16]	9.92	17.6	160	≥ 0.11	$2.00 \pm 0.04 \pm 0.14$	$70.07 \pm 0.02 \pm 5.26$
Pal et al. [17]	19.07	16.38	S.L.	≥ 0.280	2.15 ± 0.01	62.17 ± 0.05
Present data	19.07	16.38	S.L.	≥ 0.255	$2.10 \pm 0.05 \pm 0.25$	$66.70 \pm 0.36 \pm 1.50$

in cross positions. We also explore less time consuming methods to connect the position with the measured time. We propose three track quality parameters which are applied to obtain a clean muon spectrum. We optimize the distances between the bars to have accurate zenith angle measurements. For the most optimal distances among the bars, the zenith angle coverage is 0-45 degrees which could be extended upto 60 degrees with reasonable precision. With our improved analysis we demonstrate that a setup of 3 bars can also be used for quick and precise measurements. The vertical muon flux measured is $66.70 \pm 0.36(stat) \pm 1.50(sys) / m^2 / sr / s$ with $n = 2.10 \pm 0.05(stat) \pm 0.25(sys)$ in $\cos^n \theta$ at the location of Mumbai, India (19° N, 72.9° E) at Sea level at a muon momentum above 255 MeV/c. The muon flux has dependence on various factors, the most prominents are latitude, altitude and a simple and portable setup like this is beneficial for such measurements at various locations. The setup is capable of distinguishing downgoing and upgoing tracks, protons and muon induced neutrons which will be explored in the near future.

Acknowledgments

We would like to thank Dr. Vineet Kumar for initial help in the detector setup and discussions. We thank Dr. Prakash Rout, Dr. Sandeep Joshi and Prof. Gobinda Majumder for many fruitful discussions and help during the measurements.

References

- [1] The Review of Particle Physics, P.A. Zyla et al. (Particle Data Group), Prog. Theor. Exp. Phys. 2020, 083C01 (2020) and 2021 update.
- [2] P.K.F. Grieder, Cosmic rays at earth: Researcher's reference manual and data book, Elsevier (2001).
- [3] B. Rossi, Interpretation of Cosmic-Ray Phenomena, Rev. Mod. Phys. **20**, 537 (1948).
- [4] P. Shukla and S. Sankrith, Int. J. Mod. Phys. A **33**, 1850175 (2018).
- [5] P. J. Hayman and A. W. Wolfendale, Proceedings of the Physical Society, 80(3), 710 (1962).

- [6] K. Greisen, The intensities of the hard and soft components of cosmic rays as functions of altitude and zenith angle, *Phys. Rev.* **61**, 212 (1942).
- [7] R. J. R. Judge and W. F. Nash, Measurements on the Muon Flux at Various Zenith Angles, *Nuovo Cimento* **35**, 999 (1965).
- [8] J. N. Crookes and B. C. Rastin, An investigation of the absolute intensity of muons at sea-level, *Nucl. Phys. B* **39**, 493 (1972).
- [9] S. Haino et al., *Phys. Lett. B* 594, 35 (2004). [astro-ph/0403704].
- [10] S. Fukui, T. Kitamura and Y. Murata, On the range spectrum of μ -mesons at sea-level at geomagnetic latitude 24N, *J. Phys. Soc. Jpn.* **12**, 854 (1957).
- [11] O. C. Allkofer, R. D. Andresen, and W. D. Dau, The muon spectra near the geomagnetic equator, *Can. J. Phys.* **46**, S301 (1968).
- [12] N. Agafonova *et al.* [OPERA], *Eur. Phys. J. C* **25** 67 (2010).
- [13] N. Karmakar, A. Paul and N. Chaudhuri, Measurements of absolute intensities of cosmic-ray muons in the vertical and greatly inclined directions at geomagnetic latitudes 16°N, *Nuovo Cim. B* **17**, 173 (1973).
- [14] M. S. Sinha and N. Basu, *Indian J. Phys.* **33**, 335 (1959).
- [15] A. K. De, P. Ghosh, S. Mitra, P. C. Bhattacharya and A. K. Das, *J. Phys. A* **5**, 1236 (1972).
- [16] S. Pethuraj, V. M. Datar, G. Majumder, N. K. Mondal, K. C. Ravindran and B. Satyanarayana, Measurement of cosmic muon angular distribution and vertical integrated flux by 2m×2m RPC stack at IICHEP-Madurai, *J. Cosmol. Astropart. Phys.* **09**, 021 (2017).
- [17] S. Pal, B. Acharya, G. Majumder, N. Mondal, D. Samuel, B. Satyanarayana, Measurement of integrated flux of cosmic ray muons at sea level using the INO-ICAL prototype detector, *J. Cosmol. Astropart. Phys.* **07**, 033 (2012).
- [18] Y. C. Wu, X. Q. Hao, Q. Yue, Y. J. LI, J. P. Cheng, K. J. Kang, Y. H. Chen, J. Li, J. M. Li and Y. L. Li, *et al.* *Chin. Phys. C* **37** (2013).
- [19] M. K. Sharan et al., *Nucl. Inst. Methods*, **994**, 165083 (2021).
- [20] E. W. Blackmore, M. Stukel, M. Trinczek, C. Slayman, S. Wen, and R. Wong, *IEEE TRANS. NUCL. SC.* 62, 6 (2015).
- [21] J. W. Lin, Y. F. Chen, R. J. Sheu and S. H. Jiang, *Nucl. Inst. Meth. A* **24**, 619 (2010).
- [22] M. Bahmanabadi, *Nucl. Inst. Meth. A* **1**, 916 (2019).
- [23] Y. Kuo, Determination of the Angular Distribution of Cosmic Rays at Sea Level, Thesis, B.Sc., MIT (2010).